applied sciences

MDPI

Article

A Monte Carlo Study of Gray-Level—Depth Mapping in Underwater Images

Zhengyu Liu, Siguang Zong, Jing Cao * and Mengxue Lin

Naval University of Engineering, Wuhan 430034, China; lin_mx_lucky@163.com (M.L.)
* Correspondence: m25385402@nue.edu.cn

Abstract

Conventional underwater images offer an accessible means of observing vertical light attenuation, but interpreting their gray-level trends requires a link between optical transport and digital image formation. This study derives conditions under which a log-linear gray-level–depth relationship is retained and evaluates trend preservation using a Monte Carlo model coupling photon transport, camera response, and 8-bit quantization. The framework provides a physical basis for interpreting the empirical gray-level attenuation slope, k_G, and identifies low-signal conditions that compromise its interpretation. In the numerical experiment, the mean relative slope difference between the virtual-camera response and an unscattered direct downwelling irradiance reference was 0.5091%, indicating agreement within the model. Field application in the freshwater Danjiangkou Reservoir identified log-linear gray-level–depth trends in four signal-qualified image sequences, whereas low-signal sequences exhibited pronounced compression of the available gray-level range. These findings support conventional cameras as a potentially low-cost complement to radiometric profiling for relative optical-attenuation monitoring.

Keywords: underwater optical imaging; diffuse attenuation coefficient of downwelling irradiance; Monte Carlo radiative-transfer simulation; digital camera imaging; log-linear regression; freshwater

1. Introduction

Vertical light attenuation governs underwater visibility and the light available to aquatic ecosystems, making its observation relevant to underwater imaging and environmental monitoring. The diffuse attenuation coefficient of downwelling irradiance, K_d, describes the depth dependence of the underwater irradiance field [1,2]. Calibrated profiling radiometers provide these measurements, supported by appropriate optical design and stray-light control [3]. Such observations inform assessments of underwater light availability and ocean-color products [4,5]. Their instrumentation, calibration, and deployment requirements also motivate complementary approaches that make optical observations more accessible in local waters.

Satellite remote sensing and lidar have extended optical observations across larger areas and provided additional information on the vertical structure. Oelker et al. retrieved underwater attenuation using ultraviolet and blue-band satellite measurements [6], while other studies investigated vertical variations in attenuation from remote-sensing observations [7]. Comparisons with BGC-Argo measurements show that retrieval performance depends on water conditions, training data coverage, and the treatment of solar geometry [8]. Lidar provides depth-resolved observations, although attenuation retrieval requires

Check for updates

Academic Editor: Marco Genovese

Received: 1 August 2026
Revised: 21 September 2026
Accepted: 22 September 2026
Published: 24 September 2026

Copyright: © 2026 by the authors. Licensee MDPI, Basel, Switzerland. This article is an open access article distributed under the terms and conditions of the Creative Commons Attribution (CC BY) license.

consideration of multiple scattering, return-signal quality, and retrieval assumptions [9–11]. These developments broaden observational capabilities, while leaving a practical need for readily deployable observations of vertical attenuation trends in local waters.

Conventional cameras offer a promising route to such observations. Castillo-Ramírez et al. demonstrated the use of digital images to estimate surface-water optical parameters [12]. Miglino et al. showed the potential of image processing for continuous river turbidity monitoring [13]. These studies establish the value of images as accessible optical observations. Extending this approach to underwater depth profiles requires a physical interpretation of the measured gray-level changes. Underwater image intensity reflects absorption and scattering, path radiance, scene composition, viewing geometry, and camera response [14–16]. Establishing how these processes jointly shape the gray-level–depth relationship is therefore central to interpreting image-derived attenuation.

Digital image processing adds another component to this relationship. DeepAquaEnhance uses hierarchical attention and adaptive feature fusion [17], while Water-Net combines image inputs produced through different enhancement operations [18]. UColor integrates multiple color spaces with transmission guidance [19], and U-Shape Transformer models spatial and cross-channel interactions [20]. These methods improve underwater visual quality, but their transformations can also modify the intensity relationships used in attenuation analysis. Nonlinear or image-dependent processing can change channel contributions and gray-level statistics, potentially altering the fitted depth trend. Related research examines phase processing in digital holographic microscopy [21], image denoising [22], and programmable lens-less imaging [23]. Other work addresses low-light enhancement [24] and neural light-field reconstruction [25]. Together, these advances highlight the need to consider optical transport and digital image formation jointly. For attenuation monitoring, the central question is under what conditions do the combined processes preserve a depth-dependent trend in image gray levels.

This study addresses that question through theoretical analysis and Monte Carlo simulation, supported by a freshwater field experiment.

The main contributions of this study are as follows:

1. A conditional interpretation of the gray-level–depth relationship distinguishes the empirical slope k_G, the simulated direct downwelling irradiance reference, and the diffuse attenuation coefficient K_d.
2. A simplified Monte Carlo imaging model assesses agreement with the direct downwelling reference and distinguishes sampling variability from 8-bit quantization effects under the specified configuration.
3. Freshwater images from the Danjiangkou Reservoir demonstrate within-sequence gray-level trend estimation and the need to diagnose low-signal compression before interpreting fitted slopes.

2. Theory and Monte Carlo Simulation

2.1. Theoretical Relationship Between Optical Attenuation and Image Gray Level

Conventional measurements of K_d generally use a radiometrically calibrated underwater profiling radiometer to acquire the vertical profile of spectral downwelling irradiance $E_d(z)$, from which K_d is calculated as the negative rate of change of its logarithm with depth. The Monte Carlo simulation follows the same logarithmic-slope formulation but uses the profile slope of the simulated direct downwelling component $E_d(z)$ as an internal model reference for comparison with the gray-level–depth slope of the virtual camera.

Within a restricted spectral band and a locally near-homogeneous water layer, if K_d varies only weakly with depth, the downwelling irradiance $E_d(z)$ can be expressed as:

$$E_d(z) = E_d(0)\exp(-K_d z) \tag{1}$$

Downwelling irradiance in Equation (1) is the cosine-weighted integral of radiance over the downwelling hemisphere. The camera records a directionally and spectrally weighted response to scene radiance within its field of view. For the j-th image frame at depth z, let $L_{\mathrm{cam},j}(x, y; z)$ denote the effective radiance entering the camera from the scene element corresponding to pixel position (x, y). The general observation model for the digital gray level can then be written as

$$G_j(x, y, z) = Q\{f[tL_{\mathrm{cam},j}(x, y, z)] + B + \varepsilon_j(x, y, z)\} \tag{2}$$

where t is an exposure-related factor; $f(\cdot)$ is the response function incorporating the sensor, gain, and in-camera processing; B is the black level; $Q\{\cdot\}$ denotes digital quantization; and ε_j represents readout noise, photon noise, and other random perturbations. The effective camera radiance L_{cam} combines the scene contribution transmitted along the viewing path with path radiance generated by scattering into that path. Downwelling irradiance E_d describes the depth-dependent illumination. Absorption and out-scattering attenuate the scene contribution, while scene reflectance, viewing geometry, and spectral response determine its effective weighting [26–29].

Within an individual image sequence, the exposure, gain, white balance, camera orientation, and image-processing workflow must remain fixed. In addition, the following conditions must be satisfied: the camera is approximately linear within the effective signal range; the black level is stable and does not dominate the relative signal; the images are not markedly underexposed or saturated; and changes in field-of-view composition do not dominate the variation in whole-image gray level. The scene illumination should also follow the approximately exponential depth dependence described above, while the effective scene-reflectance and viewing-path factors remain approximately depth-invariant. The path-radiance contribution should be negligible relative to the scene contribution or vary approximately in proportion to it over the fitted depth interval. Under these optical and camera-response conditions, the gray-level statistic $G^*(z)$, aggregated from multiple frames at the same depth, can be approximated as

$$G^*(z) \approx G_0^* \exp(-k_G z) \tag{3}$$

The equivalent regression form with a free intercept is

$$\ln G^*(z) = \beta_0 - k_G z + \varepsilon_z \tag{4}$$

where β_0 is the free intercept, ε_z is the logarithmic residual at the depth-point level, and k_G is the empirical gray-level attenuation slope in m^{-1}. Equations (3) and (4) constitute a conditional image-domain model; only when the imaging and signal conditions described above are satisfied can the empirical gray-level attenuation slope characterize the optical attenuation trend in the water. The magnitude of k_G remains dependent on the scene, spectral band, camera response, and processing workflow. Relating this image-domain slope quantitatively to the diffuse attenuation coefficient requires radiometric calibration and independent validation under matched spectral and observational conditions.

2.2. Monte Carlo Photon Propagation and Numerical Imaging Configuration

To examine the effects of stochastic propagation, absorption, scattering, finite-receiver effects, and digital quantization on the image-domain relationship, a Monte Carlo (MC) radiative-transfer model is constructed. The simulated direct downwelling irradiance and the virtual camera share the same water optical parameters. Photons are incident on the air–water interface at a zenith angle of 30° and an azimuth angle of 0°, with refraction and interface losses treated using Snell's law and the Fresnel equations.

The photon free path ℓ is determined by the extinction coefficient c

$$l = \frac{-\ln \xi}{c} = \frac{-\ln \xi}{a+b},\ \xi \sim U(0,1) \tag{5}$$

where a is the absorption coefficient and b is the scattering coefficient. After each collision, the propagation direction is resampled according to the Henyey–Greenstein phase function [30], and the photon weight is updated using the scattering ratio b/c. Photon tracking terminates when a photon escapes through the water surface, reaches the lower boundary of the computational domain, is captured by the receiving plane of the virtual camera, has a weight below 1×10^{-5}, or reaches 100 collisions. The main parameters are listed in Table 1, and the state transitions and termination criteria are shown in Figure 1.

The numerical experiment records two statistical outputs that share the same water optical parameters, solar geometry, and stochastic propagation process. The first is the simulated direct downwelling irradiance statistic E_d, calculated from the weighted contributions of unscattered photons crossing the tally planes at each depth in the downward direction; it serves as the internal reference for vertical attenuation in the model. The second is the virtual camera response, calculated from the weights of photons that hit the active sensor area. A continuous pre-quantization response DN_{float} is first calculated, then rounded and clipped to obtain DN_8, the digital-number (DN) response corresponding to a conventional 8-bit image. DN_{float} is used only to distinguish the effect of the continuous response from that of 8-bit quantization, whereas the main trend analysis uses DN_8. The virtual camera is configured with reference to an MV-CS016-10GC color industrial camera and a Sony IMX296 sensor: the resolution is 1440 × 1080, the pixel size is 3.45 μm, the effective sensor dimensions are approximately 4.968 mm × 3.726 mm, the quantum efficiency is 55%, the gain is 24 dB, and the digital output is 8-bit. Photons that hit the camera body without entering the active sensor area are recorded as non-imaging hits.

Table 1. Main optical parameters and termination criteria used in the Monte Carlo numerical experiment.

Parameter	Representative Setting for Lake Water	Role
Absorption coefficient a (m^{-1})	0.100	Absorption loss in the medium
Scattering coefficient b (m^{-1})	0.300	Scattering intensity in the medium
Extinction coefficient c (m^{-1})	0.400	c = a + b
Henyey–Greenstein anisotropy factor g	0.85	Scattering-angle sampling
Refractive index of water n	1.333	Refraction calculation
Solar incidence angle on the air side	30°	Incident geometry
Termination weight	1×10^{-5}	Low-weight termination
Maximum number of collisions	100	Long-path truncation

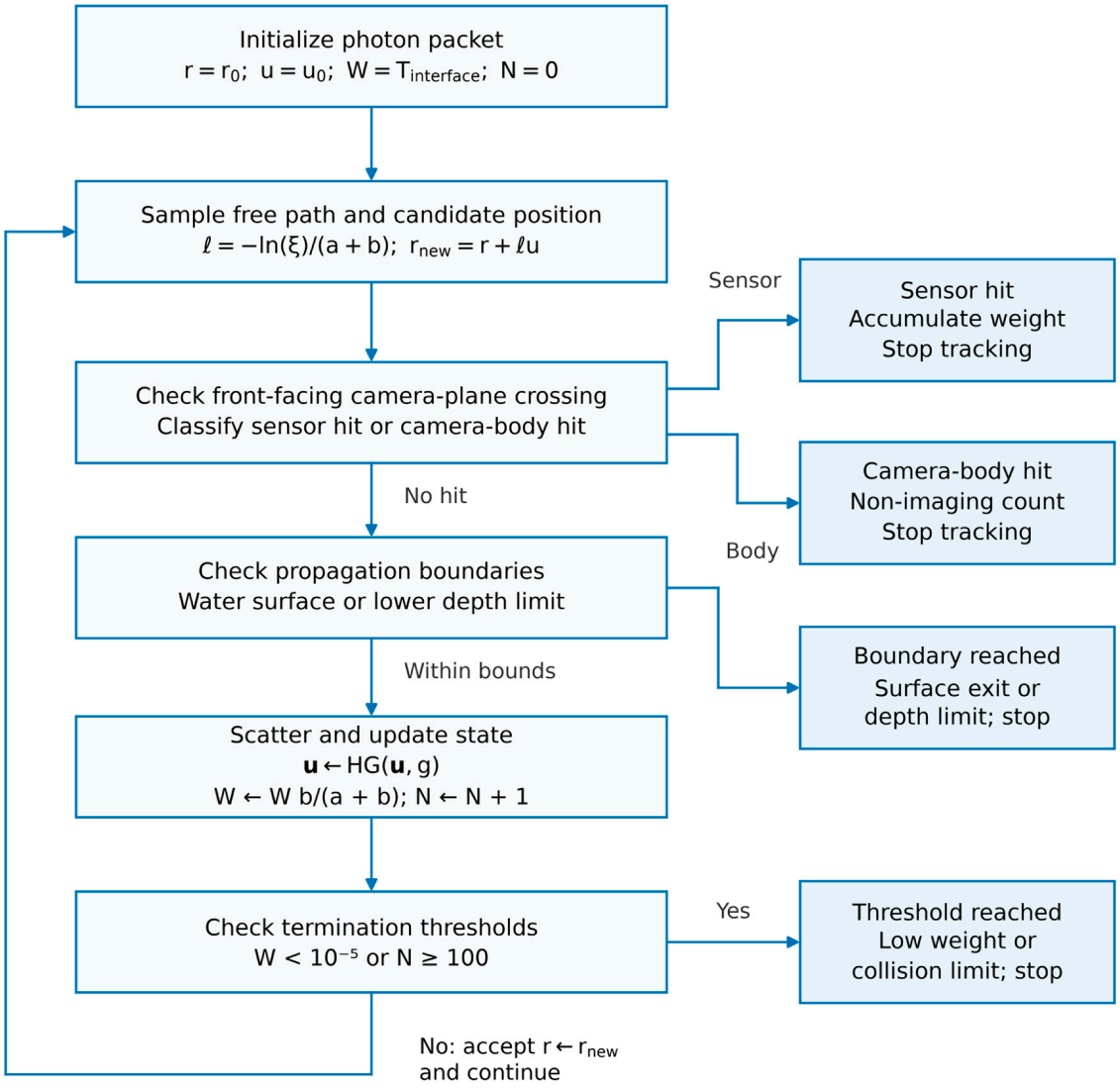


Figure 1. State machine for Monte Carlo photon transport and virtual imaging. The workflow includes photon initialization, propagation, scattering, weight updating, and termination after a sensor or camera-body hit, escape, a depth-limit crossing, a low-weight event, or attainment of the maximum collision count.

The two outputs are fitted separately as follows:

$$E_{\mathrm{MC}}(z) = A_E \exp(-K_{\mathrm{MC},E} z) \tag{6}$$

$$G_{\mathrm{MC}}(z) = A_G \exp(-k_{G,\mathrm{MC}} z) \tag{7}$$

The relative difference between the slopes is used to quantify trend consistency within the model

$$\delta_s = \left| \frac{k_{G,\mathrm{MC}} - K_{\mathrm{MC},E}}{K_{\mathrm{MC},E}} \right| \times 100\% \tag{8}$$

where $K_{\mathrm{MC},E}$ denotes only the reference slope of the direct downwelling component in the model. To assess Monte Carlo sampling noise and numerical convergence, the number of photon packets is increased from 1×10^5 to 1×10^6 packets per depth in increments of 1×10^5; each sampling level is repeated using 10 independent random seeds. At the highest sampling level, the main analysis compares the means, between-replicate dispersion, log-linear trends, and relative slope differences of the simulated direct downwelling irradiance reference slope and the 8-bit virtual-camera gray-level attenuation slope.

A separate factorial analysis combines 45 settings of the absorption-to-extinction ratio a/c (0.1125–0.50), the Henyey–Greenstein parameter g (0.85–0.92), and solar zenith angle (10°–60°), with extinction fixed at c = 0.400 m^{-1}. Each setting uses 10 independent repeats with 10^6 photons per depth. The mean camera-derived slope across repeats is compared with the analytical direct-component reference Kref = c/cos(θw), where θw is calculated using Snell's law with a water refractive index of 1.333. The relative difference is calculated from the scenario mean slope, whereas Equation (8) evaluates differences within individual repeats.

2.3. Numerical Convergence of the Monte Carlo Simulation

Figure 2 shows the changes in fitted slope and depth-specific deviation as the sample size increases. Both slopes remain close to 0.431 m^{-1}, while the standard deviation among repeated camera-response simulations is larger and decreases at the high-sampling end. The median deviation of DN_8 from the reference decreases from 2.29% at 1×10^5 photon packets to 1.25% at 1×10^6, and the 95th percentile decreases from 11.61% to 5.15%. The changes level off after approximately 6–8 $\times$ 10^5 packets; therefore, 1×10^6 photon packets per depth and 10 replicates are used in the subsequent analysis.

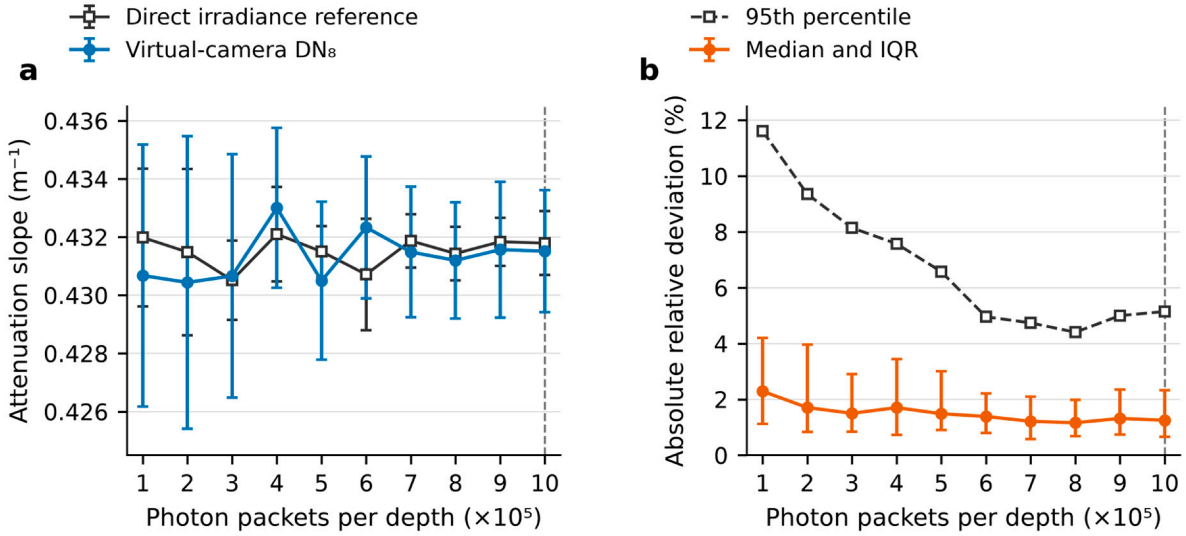


Figure 2. Stability of the slopes and depth trends in the MC numerical experiment at different numbers of photon packets. (**a**) Fitted slopes of the simulated direct downwelling irradiance reference and the 8-bit virtual-camera response; symbols indicate means, and error bars indicate ±1 standard deviation across 10 independent replicates. (**b**) Absolute relative deviation of DN_8 from the reference, pooled across 10 independent replicates and depths of 1–11 m after excluding the 0.003 m normalization anchor. The orange points and error bars indicate the median and interquartile range, respectively, and the black dashed line with square markers indicates the 95th percentile. The vertical dashed line marks the setting of 1×10^6 photon packets per depth.

The number of effective camera hits increases with the number of photon packets. Under finite-aperture collection at greater depths, only a small number of pixels contribute to the quantized gray-level statistic, leading to greater dispersion in the deviations. Local fluctuations at the high-sampling end are consistent with stochastic fluctuations under weak-signal conditions. Within approximately 6×10^5 to 1×10^6 photon packets per depth, further increases in the photon count do not produce a consistent reduction in error.

2.4. Preservation of the Attenuation Trend After Digital Quantization

Figure 3 shows that both normalized signals decrease from the surface to 11 m, with approximately parallel semi-logarithmic curves. The depth-specific deviation is smaller in shallow water and becomes more dispersed at 11 m. In Table 2, the reference slope and the 8-bit response slope are 0.43179 ± 0.00110 and 0.43152 ± 0.00209 m^{-1}, respectively, with a mean relative difference of 0.5091%.

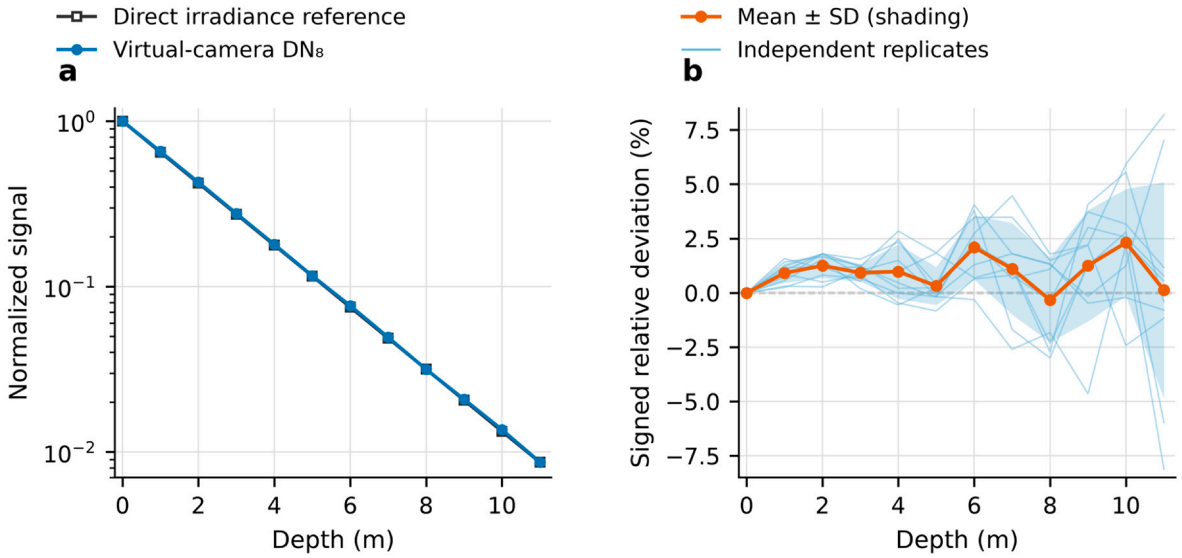


Figure 3. Comparison of the 8-bit virtual-camera response and the simulated direct downwelling irradiance reference at 1 × 10^6 photon packets per depth and 10 independent replicates. (**a**) Normalized depth profiles of the two statistics; the curves and shaded areas indicate the mean and standard deviation, respectively. (**b**) Signed depth-specific relative deviation of the 8-bit response from the reference; thin light-blue lines represent the independent replicates, while the orange curve and blue shading indicate the mean and standard deviation, respectively. The relative deviation is calculated as 100 × (DN8, norm − Ed,norm)/Ed,norm.

Table 2. Trend identifiability and quantization results from the MC numerical experiment (1 × 10^6 photon packets per depth, 10 independent replicates).

Statistical Output	Fitted Slope (m^{-1}, Mean ± Standard Deviation)	Coefficient of Determination R^2 (Mean)	Mean Relative Difference from the Reference Slope (%)	Maximum Relative Difference (%)
Simulated direct downwelling irradiance E_d	0.43179 ± 0.00110	0.999998	–	–
Virtual-camera DN_8	0.43152 ± 0.00209	0.999884	0.5091	1.2062

The approximately parallel curves are consistent with the expectation from Equations (3) and (4): when the propagation conditions are the same, the receiver geometry is fixed, and the response is approximately linear, depth-invariant multiplicative factors such as quantum efficiency, gain, and effective receiving area mainly enter the intercept after logarithmic transformation, while vertical propagation attenuation is retained in the slope term. The comparison before and after quantization shows that the mean slopes of DN_{float} and DN_8 are 0.431668 and 0.431516 m^{-1}, respectively, a difference of 0.000152 m^{-1}; their mean relative differences from the reference slope are 0.5095% and 0.5091%, respectively. These results do not support attributing the greater dispersion at depth under the current configuration primarily to 8-bit rounding. The effective-hit weight fraction

decreases from 7.4902% near the surface to 0.0649% at 11 m as between-replicate dispersion increases. Under the present numerical configuration, this result is more consistent with a reduction in the number of effective hit samples owing to finite-receiver effects.

Across the 45 tested configurations, the maximum relative difference between the mean camera-derived slope and the analytical direct-component reference was 0.7246%.

3. Experiments

3.1. Field Imaging System and Data Acquisition

Field observations were conducted in the Danjiangkou Reservoir using an MV-CS016-10GC color industrial camera in a waterproof housing lowered by a shipborne crane to preset depths of 0–11 m. Images were acquired under natural light and near-calm surface conditions, without an external light source. The acquisition geometry and location are shown in Figure 4. The camera was mounted horizontally in the housing and allowed to stabilize before image acquisition. The housing window had an approximate transmittance of 99.7% and a thickness of about 1 cm, and the housing introduced no obstruction into the optical path. White balance was fixed during acquisition. Automatic exposure and automatic gain were disabled, and Line 0 rising-edge triggering was used. Exposure and gain followed the sequence settings listed below. Image acquisition was conducted from 11:44:33 to 12:17:59 on 10 November 2025.

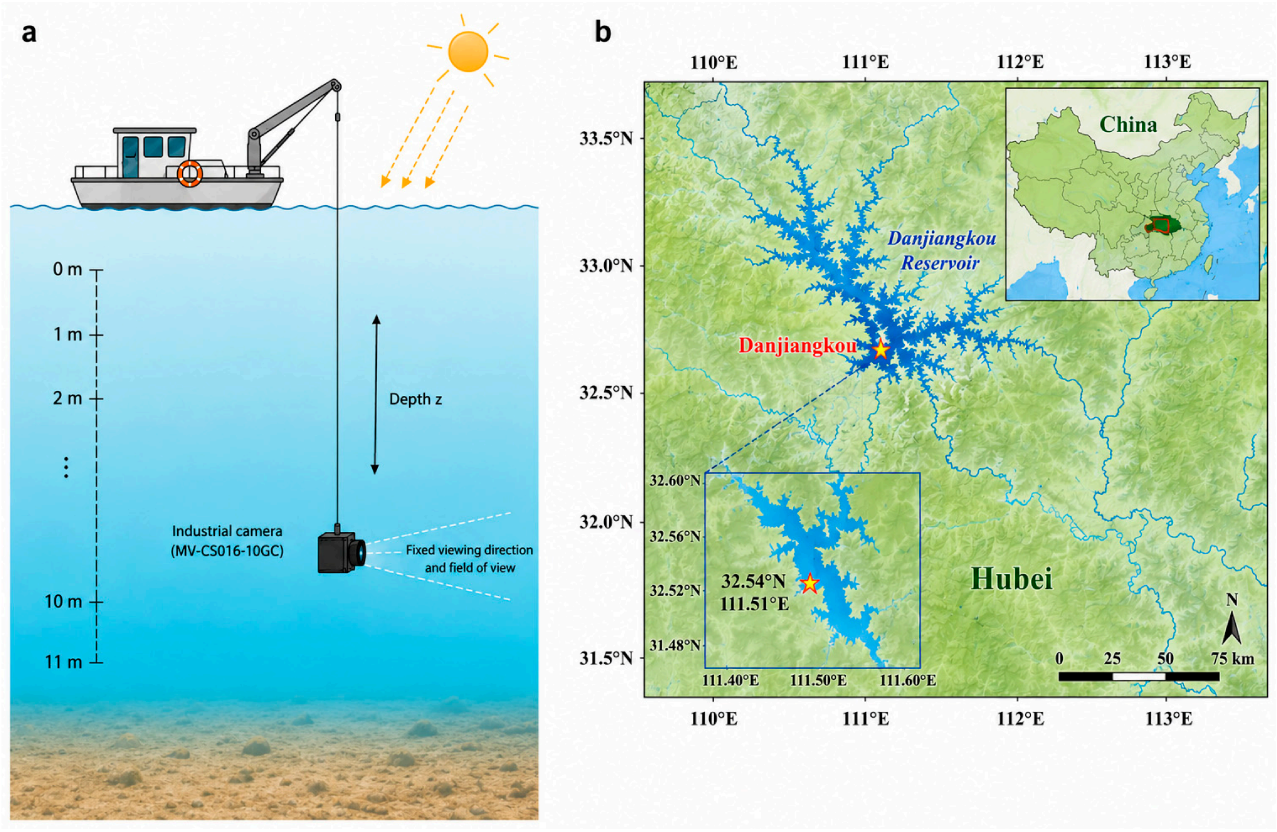


Figure 4. Field acquisition geometry and sampling location in the Danjiangkou Reservoir. (**a**) The camera was lowered from a shipborne platform to preset depths of 0–11 m and acquired images under natural sunlight with a fixed orientation and field of view. (**b**) Sampling location in the Danjiangkou Reservoir.

Maintaining a fixed attitude, orientation, field of view, exposure, and gain allows depth-invariant response terms to enter mainly into the intercept in Equation (4). Natural-light fluctuations, suspended particles, and deployment disturbances may still cause local

deviations; their effects are therefore examined using the within-depth median of multiple frames and residual analysis.

Images were recorded at depths of 1–11 m at 1 m intervals, providing 4024 frames for field-image processing. Using the criterion that each imaging condition must include at least 3 valid depth points, 3615 frames from 7 imaging conditions were included in the gray-level–depth fitting, yielding 50 depth–condition statistical points. The remaining 409 frames belonged to six other acquisition settings, each recorded at only one depth (1 or 11 m), and were not used for slope estimation. Across all acquisition settings, the numbers of frames at depths of 1–11 m were 471, 456, 342, 361, 365, 256, 431, 311, 348, 309, and 374, respectively.

The 24-dB sequences comprised 100 μs (1–5 m, 415 frames), 1000 μs (1–10 m, 797 frames), 3000 μs (2–10 m, 630 frames), and 5000 μs (7–11 m, 364 frames). The 0-dB sequences comprised 1000 μs (1–7 m, 481 frames), 3000 μs (1–9 m, 607 frames), and 5000 μs (7–11 m, 321 frames).

3.2. Image Processing and Gray-Level Statistics

The retained field images were uncompressed 24-bit BMP files with 8 bits per RGB channel; RAW or higher-bit-depth field images were not retained. The 8-bit format reduces storage, transmission, and processing requirements for lightweight field acquisition. Zero-valued and saturated pixels are evaluated as signal-quality diagnostics, including separate RGB checks. The Monte Carlo comparison of continuous and 8-bit responses evaluates quantization under the modeled imaging conditions.

For the j-th color image, a grayscale image is generated using the BT.601 luma weights [31]:

$$\mathrm{Gray}_j(x,y) = 0.299R_j(x,y) + 0.587G_j(x,y) + 0.114B_j(x,y) \tag{9}$$

where R_j, G_j, and B_j are the red-, green-, and blue-channel pixel values, respectively. In the baseline processing, the entire image serves as the region of interest (ROI), denoted by Ω, and the mean gray level within this region is used as the image-level statistic:

$$G_{\mathrm{img},j} = \frac{1}{N_\Omega} \sum_{(x,y)\in\Omega} \mathrm{Gray}_j(x,y) \tag{10}$$

Consecutive images acquired under the same imaging setting and at the same depth z form the set $J(z)$. To reduce the effects of short-term interframe illumination fluctuations, local particles, bubbles, and occasional anomalous frames, the median of the image-level mean gray levels is defined as the depth-aggregated gray level:

$$G^*(z) = \mathrm{median}\{G_{\mathrm{img},j} : j \in J(z)\} \tag{11}$$

Accordingly, subsequent regression uses only $G^*(z)$ at each depth.

3.3. Trend Estimation and Uncertainty Analysis

For each sequence, the depth-aggregated gray levels are fitted according to Equation (4) using linear regression with a free intercept. The unit of analysis is the depth point rather than the individual image frame. Normalization to the shallowest valid depth, $\frac{G^*(z)}{G^*(z_0)}$, is used only for plotting; it is not imposed as a regression constraint, and the regression line is not required to pass through the shallowest depth point. The gray-level attenuation slope is defined from the regression slope s as $k_G = -\mathrm{s}$.

Let $y_i = \ln G^*(z_i)$, with $\hat{y}_i$ denoting the fitted value, $\overline{y}$ the mean across depth points, and N the number of depth points. The goodness of fit and the errors on the logarithmic scale are defined as

$$R^2 = 1 - \frac{\sum_i (y_i - \hat{y}_i)^2}{\sum_i (y_i - \overline{y})^2} \tag{12}$$

$$\mathrm{RMSE}_{\log} = \sqrt{\frac{1}{N}\sum_i (y_i - \hat{y}_i)^2} \tag{13}$$

$$\mathrm{MAE}_{\log} = \frac{1}{N}\sum_i |y_i - \hat{y}_i| \tag{14}$$

To describe the relative deviation on the original gray-level scale, the observed-to-fitted gray-level ratio is defined as

$$B_{\mathrm{rel}}(z) = \frac{G^*(z)}{\hat{G}^*(z)} = \exp(\varepsilon_z) \tag{15}$$

and its coefficient of variation across depths is defined as

$$\mathrm{CV}_{B_{\mathrm{rel}}} = \frac{\sigma_{B_{\mathrm{rel}}}}{\mu_{B_{\mathrm{rel}}}} \times 100\% \tag{16}$$

Within-depth frame dependence is accounted for using a depth-stratified stationary block bootstrap. Frames are ordered by acquisition number and divided into segments at numbering gaps. Circular blocks with geometrically distributed lengths are resampled within each segment, preserving its frame count; expected block lengths are selected from the segment autocovariance. Each of 5000 replicates recomputes the depthwise medians, their logarithms, and the fitted slope k_{G}. The 2.5th and 97.5th percentiles define a conditional 95% interval. Halving and doubling the expected block lengths assess interval sensitivity, and separate fits to the first and second halves of each depth sequence assess temporal drift. Relative interval width is calculated as the interval width divided by $|k_{\mathrm{G}}|$ and multiplied by 100%.

The leave-one-depth-out analysis removes one depth point at a time and re-estimates $k_{G,(-i)}$, using

$$S_{\mathrm{LODO}} = \max_i \left| \frac{k_{G,(-i)} - k_G}{k_G} \right| \times 100\% \tag{17}$$

to describe whether the slope is disproportionately influenced by a single depth point. This metric is only a sensitivity diagnostic and cannot independently determine sequence reliability.

Depth-level heteroscedasticity is assessed using the studentized Breusch–Pagan test on the fitted log-gray residuals. HC3 covariance and a Student's t reference with n − 2 degrees of freedom provide approximate 95% regression confidence intervals, where n is the number of fitted depths. These intervals describe depth-level regression uncertainty; the block-bootstrap intervals describe frame variability conditional on the sampled depths. Variability is propagated through depth aggregation, logarithmic transformation and slope fitting in each bootstrap replicate. A separate calculation uses the variance of each log-depth median and its linear-regression weight to check the resulting slope variance. Robustness checks remove the shallowest depth, the deepest depth or both, and replace the within-image mean with the median or the 5th–95th-percentile trimmed mean while retaining BT.601 conversion, the full-image ROI, and depthwise median aggregation.

For sequences that meet the minimum number of depth points and are successfully fitted, multiple metrics are combined to diagnose signal quality. The maximum proportion of

zero-valued pixels reflects the risks of low-end quantization and underexposure; $CV_{B_{rel}}$ reflects residual dispersion across depths. S_{LODO} reflects the influence of an individual depth point; R^2 describes only how well the specified depth points conform to a linear model.

Sequences are classified using the following combined criteria: at least 3 valid depth points and a completed fit; $R^2 \geq 0.95$; $CV_{B_{rel}} \leq 15\%$; maximum relative deviation of $B_{rel} \leq 35\%$; maximum proportion of zero-valued pixels $\leq 5\%$; and monotonic gray levels (the number of upward steps may not exceed 25% of the number of depth intervals, and any single upward step may not exceed 10%). Sequences satisfying all criteria are classified as primary trend sequences; sequences that are successfully fitted but fail any criterion are classified as low-signal boundary sequences; sequences with fewer than 3 valid points are classified as not fitted. Leave-one-depth-out sensitivity is used only as an auxiliary diagnostic.

The R, G, and B channels are also analyzed separately using the same frame-level whole-image mean, depthwise median aggregation, and log-linear fitting procedure. Channel-wise zero-valued and saturated-pixel fractions are checked alongside these fits, with saturation defined as DN = 255.

3.4. Field Fitting Results and Signal Quality

Table 3 summarizes the gray-level–depth fitting parameters and signal-quality metrics for the seven sequences. In the four 24-dB sequences, logarithmic gray level decreases approximately linearly with depth, with k_G values of 0.41655–0.45091 m^{-1}, R^2 values of 0.99155–0.99789, and a maximum proportion of zero-valued pixels no greater than 3.08%. Although the model could still be fitted to the three 0-dB sequences, their maximum proportions of zero-valued pixels are 64.06–96.22%, and their coefficients of variation for the observed-to-fitted gray-level ratio are 16.84–46.80%, consistent with compression of the effective gray-level range under low-signal conditions. This feature is also consistent with the differences in raw-image brightness shown in Figure 5. According to the combined rules above, the four 24-dB sequences are classified as primary trend sequences, whereas the three 0-dB sequences are classified as low-signal boundary sequences because at least one criterion is not satisfied. The 1000 µs and 5000 µs sequences at 0 dB simultaneously have an R^2 below 0.95, $CV_{B_{rel}}$ above 15%, and a maximum proportion of zero-valued pixels above 5%; for the 3000 µs sequence, the principal failed criteria are $CV_{B_{rel}}$ and the maximum proportion of zero-valued pixels.

Table 3. Gray-level–depth fitting results and signal-quality diagnostics for the sequences included in the analysis.

Exposure/Gain (µs/dB)	Empirical Slope k_G (m^{-1})	R^2	CV of Observed/Fitted Ratio (%)	Maximum Zero-Valued Pixels (%)	Leave-One-Depth-Out Sensitivity (%)	Sequence Classification
100/24	0.41655	0.99155	6.09	2.39	9.21	Primary trend
1000/0	0.64977	0.91750	36.38	92.57	22.55	Low-signal boundary
1000/24	0.45063	0.99397	10.67	3.08	2.30	Primary trend
3000/0	0.51007	0.98543	16.84	64.06	5.82	Low-signal boundary
3000/24	0.43736	0.99669	6.89	0.00	2.05	Primary trend
5000/0	0.92576	0.90644	46.80	96.22	31.57	Low-signal boundary
5000/24	0.45091	0.99789	3.26	0.00	4.20	Primary trend

At 5000 µs, both gain settings cover the same depth range of 7–11 m. The slope at 0 dB is 0.92576 m^{-1}, greater than the value of 0.45091 m^{-1} at 24 dB, but the maximum proportion of zero-valued pixels reaches 96.22%. Thus, the larger slope is accompanied by low-end signal compression and cannot be interpreted as a more reliable attenuation estimate. The

1000 and 3000 µs groups show the same directional pattern but cover different depth ranges and are therefore used only as supporting evidence. Although the R^2 of the 3000 µs/0 dB sequence is 0.98543, this does not establish the physical interpretability of its slope.

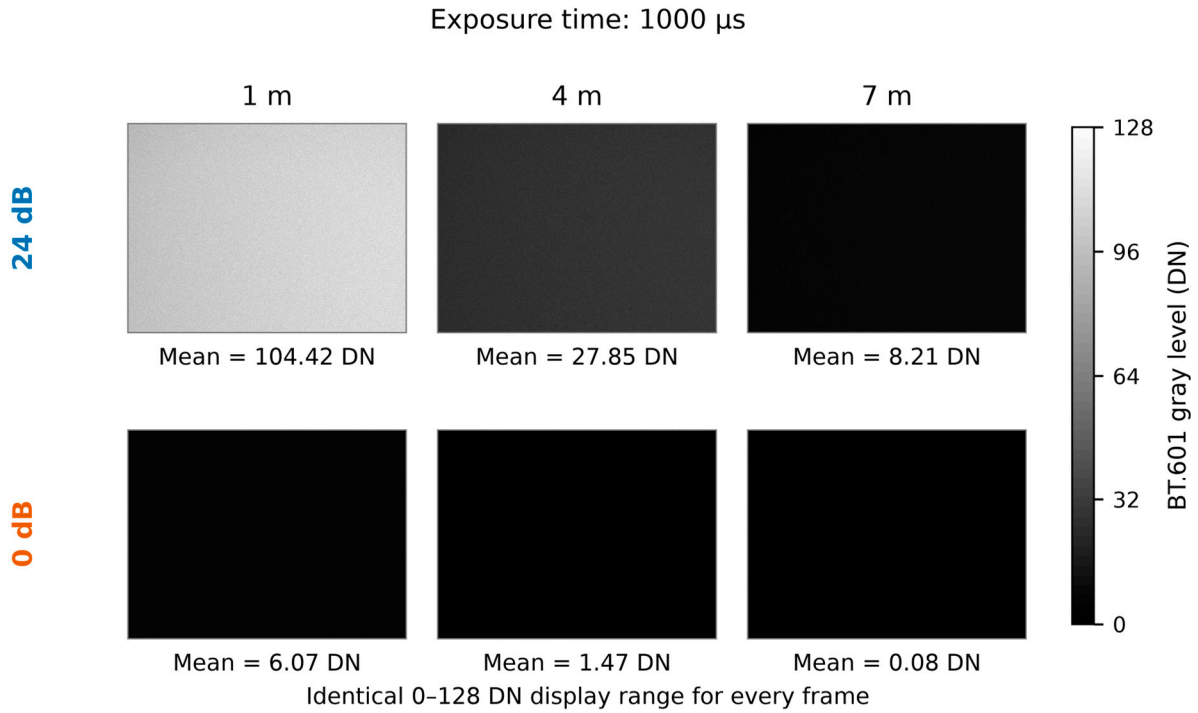


Figure 5. Representative frames from the 24-dB and 0-dB sequences at 1000 µs. The upper row shows 24 dB, and the lower row 0 dB; the columns correspond to depths of 1, 4, and 7 m. Each image is the frame whose whole-image mean gray level is closest to the median at that depth, and all images use the same BT.601 conversion and a display range of 0–128.

The B-channel slopes exceeded the R-channel slopes in all four primary 24-dB sequences, with B/R ratios of 1.080–1.244 (Table 4). Interpretation of these broadband slopes also requires consideration of the scene spectrum, camera spectral sensitivity, and image processing. Table 5 reports the maximum zero-valued and saturated-pixel fractions for each sequence. In the 3000 µs/24 dB sequence, 65.55–69.52% of G-channel pixels were saturated in each of the 85 frames recorded at 2 m, although the composite grayscale remained unsaturated. Restricting the fit from 2–10 m to 3–10 m increased the grayscale and G-channel slopes by 1.64% and 2.06%, respectively. Table 4 retains the 2–10 m estimates because removing the 2 m observations changes both the fitted depth range and the contribution of clipped images.

Table 4. Channel-specific attenuation slopes and coefficients of determination for the four 24-dB sequences. All slopes are in m^{-1}; the depth interval is the same for all three channels within each sequence.

Exposure (µs)	Depth (m)	$k_{G,R}$	R^2_R	$k_{G,G}$	R^2_G	$k_{G,B}$	R^2_B	Slope Ratio B/R
100	1–5	0.36049	0.95091	0.43367	0.99267	0.44861	0.97801	1.244
1000	1–10	0.46329	0.98237	0.44067	0.99334	0.51721	0.98216	1.116
3000	2–10	0.45170	0.99696	0.42624	0.99513	0.54290	0.99677	1.202
5000	7–11	0.44191	0.99568	0.45211	0.99772	0.47722	0.99154	1.080

Table 5. Maximum within-frame percentages of zero-valued and saturated channel pixels across the seven fitted sequences.

Exposure/Gain (μs/dB)	R = 0 (%)	G = 0 (%)	B = 0 (%)	G = 255 (%)
100/24	20.72	3.97	39.62	0.00
1000/24	32.83	4.08	47.31	0.00
3000/24	3.75	0.00	73.58	69.52
5000/24	2.37	0.00	21.93	0.00
1000/0	94.59	92.59	96.61	0.00
3000/0	93.84	64.09	99.52	0.00
5000/0	96.76	96.32	99.25	0.00

Each entry is the maximum within-frame percentage over the corresponding sequence. Zero-valued and saturated pixels are defined by channel values of 0 and 255, respectively. No saturation was detected in the R or B channels or in the composite BT.601 grayscale.

3.5. Effects of Low-Signal Conditions

Figure 5 compares representative 1000 μs frames at the two gain settings. At depths of 1, 4, and 7 m, the mean gray levels are approximately 104.4, 27.9, and 8.2 at 24 dB, compared with 6.1, 1.5, and 0.1 at 0 dB; the 7 m image in the latter group is nearly black. The two groups use the same exposure time (1000 μs), BT.601 conversion, and 0–128 display range, excluding display stretching as the cause of the visual difference. The 0 dB sequence also exhibits compression of the effective gray-level range.

The reduction in effective gray levels is associated with the input signal approaching the lower limit of 8-bit quantization. The minimum step of each RGB channel is 1 DN, and BT.601 conversion cannot recover information below the quantization limit. The 0-dB sequences enter the lowest quantization range at shallower depths; at 1000 μs and 7 m, the maximum proportion of zero-valued pixels reaches 92.57%. Once a large number of pixels are quantized to zero, the image response departs from the multiplicative relationship in Equation (3), and the log-linear regression slope may be distorted. It therefore cannot be interpreted as evidence of stronger attenuation in the water.

3.6. Exposure Response and Trend Robustness

Figure 6a shows that, at 24 dB, the four sequences acquired at 100 μs (1–5 m), 1000 μs (1–10 m), 3000 μs (2–10 m), and 5000 μs (7–11 m) all decrease approximately linearly with depth after being normalized to their respective shallowest valid depth z_0; the fitted slopes k_G range from 0.41655 to 0.45091 m^{-1}. The curves start at different positions on the depth axis because each is normalized to its own shallowest valid depth; this does not imply that they have the same gray level at the same absolute depth. Figure 6b compares representative frames at a fixed depth of 7 m and gain of 24 dB for exposure times of 1000, 3000, and 5000 μs. The three frames use the same BT.601 grayscale conversion and 0–128 DN display range. Their whole-image mean gray levels are 8.21, 26.54, and 44.21 DN, respectively, and increase with exposure time.

Within the operating range that is neither saturated nor close to the zero-value quantization region, the effect of exposure time is approximated as a change in the multiplicative baseline of the image gray level: $G(z,t) \approx C(t)\exp(-k_G z)$, where C(t) increases with exposure time. At 7 m, the ratio of the three exposure times is 1:3:5, whereas the ratio of the mean gray levels is approximately 1:3.23:5.38. The gray-level-to-exposure-time ratios are 0.00821, 0.00885, and 0.00884 DN/μs, respectively, consistent with an approximately proportional gray-level response to exposure time within the range of these data. Normalizing each exposure sequence separately removes C(t), allowing the relative depth-attenuation trends to be compared. Exposure time nevertheless determines the usable depth window: if the

exposure is too short, the deeper signal enters the low-end quantization region. If it is too long, shallow images may be overexposed. Once zero-value compression or saturation occurs, the multiplicative relationship no longer holds and the fitted slope may deviate. Thus, the results in Figure 6 are consistent with the processing logic of maintaining fixed imaging conditions, normalizing each sequence separately, and jointly checking the dynamic range, but they do not demonstrate that absolute gray levels or k_G values obtained under different exposure conditions are interchangeable physical quantities.

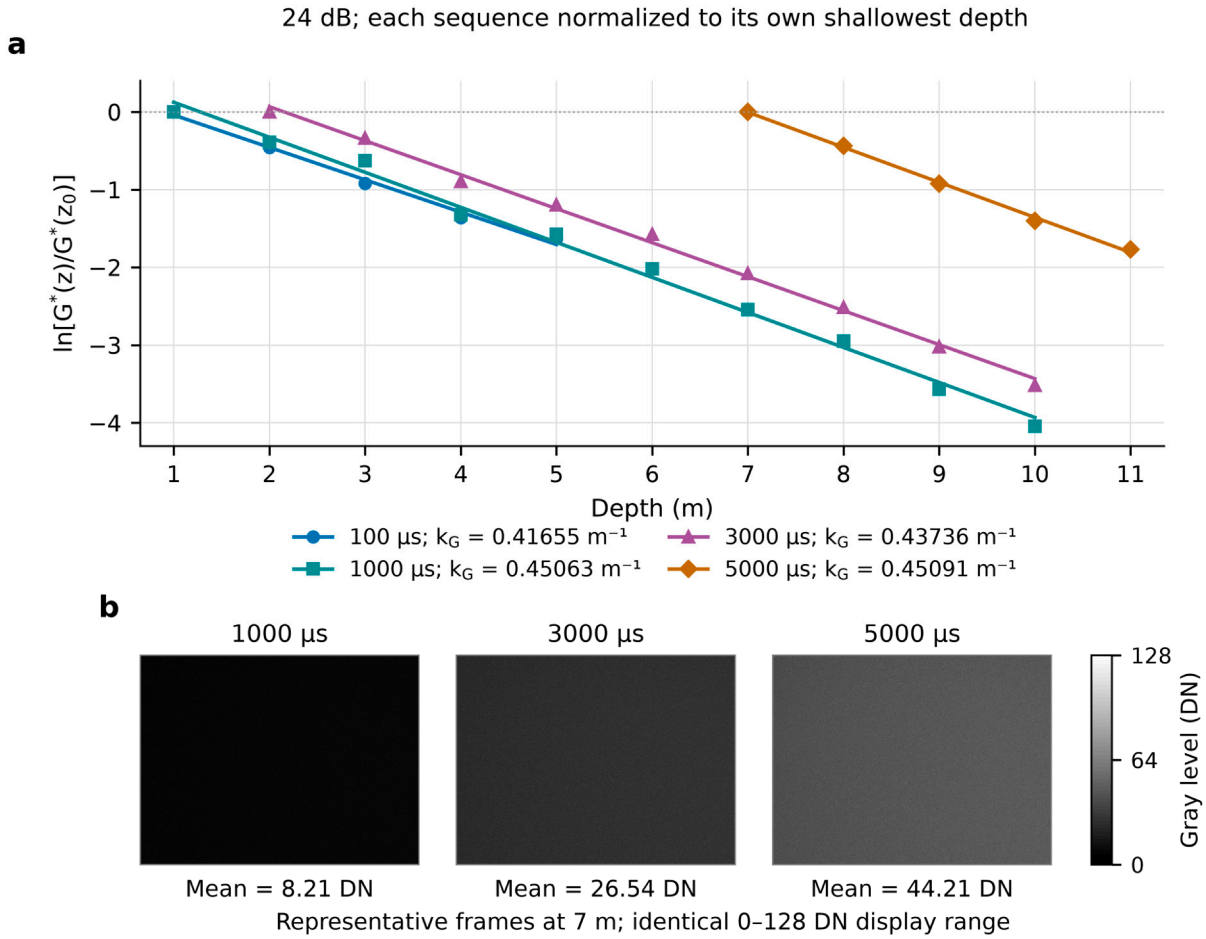


Figure 6. Effect of exposure time on the field gray-level–depth relationship. (**a**) Gray-level–depth relationships for the four 24-dB sequences, each normalized to its own shallowest valid depth. Symbols show depthwise median gray levels after log normalization; lines show the corresponding free-intercept regressions. (**b**) Representative 1000, 3000, and 5000 µs frames at 7 m and 24 dB, displayed using the same BT.601 conversion and 0–128 DN range.

For the four primary 24-dB sequences, median within-depth lag-1 correlations ranged from 0.870 to 0.995 (Table 6). Their HC3 95% confidence intervals remained above zero but were wider than the conditional block-bootstrap intervals. HC3 standard errors were 1.32–2.00 times the conventional regression standard errors. For these sequences, the studentized Breusch–Pagan LM p values ranged from 0.0521 to 0.9111; HC3 was used irrespective of the diagnostic result. The HC3 interval for the 5000 µs/0 dB sequence included zero.

For the primary sequences, halving or doubling the expected block lengths gave relative interval widths of 0.21–0.98%, compared with 0.23–0.98% under the selected block lengths. Slopes fitted using the first and second halves of the frames at each depth differed by at most 0.364% of the full-sequence estimate. Removing endpoints or one depth at a

time changed the slopes by at most 9.21%. Replacing the within-image mean with the median or trimmed mean changed them by 0.17–1.12%. Across all seven fitted sequences, the relative difference between propagated and bootstrap slope standard deviations was below 0.71%.

Table 6. Slope uncertainty and within-depth temporal dependence for the seven fitted sequences.

Exposure/Gain (μs/dB)	Depth Count	Block-Bootstrap 95% Interval (m^{-1})	HC3 95% Confidence Interval (m^{-1})	Median Lag-1 Correlation
100/24	5	[0.41383, 0.41792]	[0.27496, 0.55814]	0.870
1000/24	10	[0.44985, 0.45114]	[0.41215, 0.48912]	0.962
3000/24	9	[0.43696, 0.43799]	[0.40773, 0.46700]	0.995
5000/24	5	[0.45052, 0.45156]	[0.38596, 0.51585]	0.976
1000/0	7	[0.64748, 0.65219]	[0.21220, 1.08733]	0.849
3000/0	9	[0.50826, 0.51292]	[0.42489, 0.59525]	0.986
5000/0	5	[0.92151, 0.92768]	[−0.17868, 2.03021]	0.859

Block-bootstrap intervals describe within-depth frame variability conditional on the sampled depths. HC3 intervals describe depth-level regression uncertainty. Lag-1 correlations use consecutive recorded frame IDs and are summarized by their median across depths.

Accordingly, the field results are used here to evaluate the repeatability and conditional usability of the image-derived attenuation trend, rather than to establish agreement with an independently calibrated radiometric reference.

4. Conclusions

This study develops a conditional framework linking vertical optical attenuation to image gray-level trends through theoretical analysis and Monte Carlo modeling, with supporting field observations from the Danjiangkou Reservoir. The framework connects underwater light propagation, camera response, and digital quantization to explain the conditions under which attenuation trends are retained in images. Its practical advantage is the use of conventional underwater cameras for relative optical-attenuation monitoring. Applicability depends on camera response, imaging conditions, and water optical properties; an approximately linear response, fixed acquisition settings, a stable field of view, sufficient dynamic range, and a locally near-homogeneous water layer underpin the theoretical relationship.

Under the specified numerical configuration of absorption, scattering, boundary conditions, simplified camera geometry, stochastic photon propagation, finite-receiver effects, and 8-bit quantization, the mean relative difference between the DN_8 slope and the simulated direct downwelling irradiance reference slope is 0.5091%. The simulation results show that the 8-bit virtual camera response retains the overall vertical attenuation trend of the reference under this configuration. The depth-specific deviations also show increased between-replicate dispersion under weak-signal conditions at depth.

The field analysis includes 3615 images from 7 imaging conditions and 50 depth–condition statistical points. The four 24-dB sequences exhibit identifiable gray-level–depth attenuation trends, whereas the three 0-dB sequences show compression of the effective gray-level range under low-signal conditions, indicating that signal-quality metrics are needed to delineate the method's limits of applicability.

This study covers only one freshwater reservoir (Danjiangkou) and one camera and lacks simultaneous ground-truth K_d measurements and complete radiometric calibration. Exposure settings are not identical among the sequences, and the number of depth points is limited. Future work should preserve raw or linear images, perform dark-field and radiometric calibrations, and combine simultaneous optical measurements, independent

water samples, and hierarchical statistical validation to evaluate reproducibility across different devices and water bodies, including marine environments, and ultimately establish a quantitative calibration relationship. Underwater engineering encompasses diverse assessment needs, including submarine-landslide loading on pipelines [32] and hull-girder damage under underwater explosions [33]. For practical underwater monitoring, image-derived attenuation trends should be reported together with signal-quality diagnostics and uncertainty intervals, so that environmental observations include an explicit measure of confidence. Recent work on probabilistic underwater 3-D reconstruction [34], adaptive acoustic cooperative positioning [35], and pressure-array-based attitude perception [36] offers complementary approaches to uncertainty quantification and underwater sensing. These developments motivate future integration of image-derived attenuation trends with calibrated optical measurements and other environmental sensors.

Author Contributions: Conceptualization, J.C. and Z.L.; methodology, M.L.; software, Z.L.; validation, Z.L.; resources, S.Z.; data curation, S.Z.; writing—original draft preparation, Z.L.; writing—review and editing, J.C. and M.L. All authors have read and agreed to the published version of the manuscript.

Funding: This work was supported by the National Defense Pre-Research Foundation of China (Grant No. 2025-J0JQ-JJ-0932).

Institutional Review Board Statement: Not applicable.

Informed Consent Statement: Not applicable.

Data Availability Statement: The data presented in this study are available from the corresponding author upon reasonable request.

Conflicts of Interest: The authors declare no conflicts of interest.

References

1. Begouen Demeaux, C.; Boss, E.; Tan, J.; Frouin, R. Algorithms to retrieve the spectral diffuse attenuation coefficient of light in the ocean from remote sensing. *Opt. Express* **2024**, *32*, 2507–2526. [CrossRef]
2. Kirk, J.T.O. *Light and Photosynthesis in Aquatic Ecosystems*, 3rd ed.; Cambridge University Press: Cambridge, UK, 2010.
3. Zhang, Y.; Wang, K.; Yue, W.; Liu, S.; Yu, J.; Ye, X. Optical Design and Stray Light Analysis of Underwater Spectral Radiometer. *Appl. Sci.* **2024**, *14*, 3172. [CrossRef]
4. Pawar, S.; Gonçalves-Araujo, R.; Timmermann, K. In search of light: Estimating diffuse attenuation coefficient of downwelling irradiance and its variation in optically complex shallow water habitats using Sentinel-2 imagery. *Sci. Total Environ.* **2025**, *965*, 178598. [CrossRef]
5. NASA Ocean Biology Processing Group. PACE OCI Level-3 Global Mapped Diffuse Attenuation Coefficient of Downwelling Irradiance (KD) Data, Version 3.2 [Dataset]. NASA Ocean Biology Distributed Active Archive Center (OB.DAAC). 2026. Available online: https://www.earthdata.nasa.gov/data/catalog/ob-cloud-pace-oci-l3m-kd-3.2 (accessed on 29 July 2026).
6. Oelker, J.; Losa, S.N.; Richter, A.; Bracher, A. TROPOMI-retrieved underwater light attenuation in three spectral regions in the ultraviolet and blue. *Front. Mar. Sci.* **2022**, *9*, 787992. [CrossRef]
7. Chen, L.; Zhang, J.; Pan, X.; Shi, P.; Zhang, X. Deriving the vertical variations in the diffuse attenuation coefficient of photosynthetically available radiation in the North Pacific Ocean from remote sensing. *Remote Sens.* **2023**, *15*, 3023. [CrossRef]
8. Begouen Demeaux, C.; Boss, E. Validation of remote-sensing algorithms for diffuse attenuation of downward irradiance using BGC-Argo floats. *Remote Sens.* **2022**, *14*, 4500. Correction in *Remote Sens.* **2024**, *16*, 313. [CrossRef]
9. Chen, Y.; Cui, X.; Gu, Q.; Zhou, Y.; Zhao, H.; Zhang, H.; Ma, S.; Xu, P.; Frielinghaus, H.; Wu, L.; et al. This is MATE: A multiple scattering correction retrieval algorithm for accurate lidar profiling of seawater optical properties. *Remote Sens. Environ.* **2024**, *307*, 114166. [CrossRef]
10. Eidam, E.F.; Bisson, K.; Wang, C.; Walker, C.; Gibbons, A. ICESat-2 and ocean particulates: A roadmap for calculating Kd from space-based lidar photon profiles. *Remote Sens. Environ.* **2024**, *311*, 114222. [CrossRef]
11. Zhang, Z.; Zhang, S.; Behrenfeld, M.J.; Jamet, C.; Di Girolamo, P.; Dionisi, D.; Hu, Y.; Lu, X.; Pan, Y.; Luo, M.; et al. Consistency analysis of water diffuse attenuation between ICESat-2 and MODIS in marginal sea: A case study in China Sea. *Remote Sens. Environ.* **2025**, *318*, 114602. [CrossRef]

12. Castillo-Ramírez, A.; Santamaría-del-Ángel, E.; González-Silvera, A.; Aguilar-Maldonado, J.; Lopez-Calderon, J.; Sebastiá-Frasquet, M.-T. Use of digital images as a low-cost system to estimate surface optical parameters in the ocean. *Sensors* **2023**, *23*, 3199. [CrossRef]
13. Miglino, D.; Jomaa, S.; Rode, M.; Saddi, K.C.; Isgrò, F.; Manfreda, S. Technical note: Image processing for continuous river turbidity monitoring—Full-scale tests and potential applications. *Hydrol. Earth Syst. Sci.* **2025**, *29*, 4133–4151. [CrossRef]
14. Jaffe, J.S. Underwater optical imaging: The past, the present, and the prospects. *IEEE J. Ocean. Eng.* **2015**, *40*, 683–700. [CrossRef]
15. Hao, Y.; Yuan, Y.; Zhang, H.; Zhang, Z. Underwater optical imaging: Methods, applications and perspectives. *Remote Sens.* **2024**, *16*, 3773. [CrossRef]
16. Cai, C.; Fan, Y.; Li, R.; Cao, H.; Zhang, S.; Wang, M. Underwater Degraded Image Restoration by Joint Evaluation and Polarization Partition Fusion. *Appl. Sci.* **2024**, *14*, 1769. [CrossRef]
17. Rehman, M.U.; Bakht, A.B.; Hussain, I. DeepAquaEnhance: Hierarchical multi-head attention and adaptive feature fusion for underwater image enhancement. *Ecol. Inform.* **2026**, *95*, 103771. [CrossRef]
18. Li, C.; Guo, C.; Ren, W.; Cong, R.; Hou, J.; Kwong, S.; Tao, D. An Underwater Image Enhancement Benchmark Dataset and Beyond. *IEEE Trans. Image Process.* **2020**, *29*, 4376–4389. [CrossRef]
19. Li, C.; Anwar, S.; Hou, J.; Cong, R.; Guo, C.; Ren, W. Underwater Image Enhancement via Medium Transmission-Guided Multi-Color Space Embedding. *IEEE Trans. Image Process.* **2021**, *30*, 4985–5000. [CrossRef]
20. Peng, L.; Zhu, C.; Bian, L. U-Shape Transformer for Underwater Image Enhancement. *IEEE Trans. Image Process.* **2023**, *32*, 3066–3079. [CrossRef]
21. Jiang, W.; Liu, L.; Bu, Y. Application of Deep Learning in the Phase Processing of Digital Holographic Microscopy. *Photonics* **2025**, *12*, 810. [CrossRef]
22. Zhu, M.L.; Yuan, J.H.; Kong, E.; Zhao, L.L.; Xiao, L.; Gu, D.B. Generative Adversarial Networks with Noise Optimization and Pyramid Coordinate Attention for Robust Image Denoising. *Int. J. Intell. Syst.* **2025**, *2025*, 1546016. [CrossRef]
23. Zhang, X.; Wang, B.; Li, S.; Liang, K.; Guan, H.; Chen, Q.; Zuo, C. Lensless imaging with a programmable Fresnel zone aperture. *Sci. Adv.* **2025**, *11*, eadt3909. [CrossRef]
24. Chen, B.; Yu, K.; Tang, Y.; Ding, X. A novel Retinex model for low-light image enhancement based on non-local and plug-and-play. *Inf. Sci.* **2025**, *721*, 122625. [CrossRef]
25. Liu, C.; Shi, L.; Wu, L.; Yu, K.; Qiu, J. Neural light field representation and reconstruction based on a ray displacement field. *Opt. Express* **2026**, *34*, 15468–15483. [CrossRef]
26. Schechner, Y.Y.; Karpel, N. Clear underwater vision. In Proceedings of the 2004 IEEE Computer Society Conference on Computer Vision and Pattern Recognition (CVPR 2004), Washington, DC, USA, 27 June–2 July 2004; Volume 1, pp. 536–543.
27. Akkaynak, D.; Treibitz, T. A revised underwater image formation model. In Proceedings of the 2018 IEEE/CVF Conference on Computer Vision and Pattern Recognition (CVPR), Salt Lake City, UT, USA, 18–23 June 2018; pp. 6723–6732.
28. Burggraaff, O.; Schmidt, N.; Zamorano, J.; Pauly, K.; Pascual, S.; Tapia, C.; Spyrakos, E.; Snik, F. Standardized spectral and radiometric calibration of consumer cameras. *Opt. Express* **2019**, *27*, 19075–19101. [CrossRef]
29. Buckler, M.; Jayasuriya, S.; Sampson, A. Reconfiguring the imaging pipeline for computer vision. In Proceedings of the 2017 IEEE International Conference on Computer Vision (ICCV), Venice, Italy, 22–29 October 2017; pp. 975–984.
30. Ramley, I.; Alzayed, H.M.; Al-Hadeethi, Y.; Chen, M.; Barasheed, A.Z. An overview of underwater optical wireless communication channel simulations with a focus on the Monte Carlo method. *Mathematics* **2024**, *12*, 3904. [CrossRef]
31. *ITU-R BT.601-7*; Studio Encoding Parameters of Digital Television for Standard 4:3 and Wide-Screen 16:9 Aspect Ratios. International Telecommunication Union: Geneva, Switzerland, 2017.
32. Dai, Z.; Wang, C.; Peng, R.; Jiang, M. Evaluating the impact force of submarine landslide on pipelines: Insights from flume tests and multiphase flow model analysis. *Ocean Eng.* **2026**, *352*, 124629. [CrossRef]
33. Wang, C.; Zheng, X.; Li, H.; Ji, K.; Lou, Y.; Zhu, Y. Coupling damage characteristics of hull girder with variable cross-section subjected to underwater explosion. *Thin-Walled Struct.* **2025**, *217*, 113910. [CrossRef]
34. Dai, D.; Wang, H.; Li, X.; Wu, H.; Shan, Z.; Yang, H.; Song, S. Probabilistic Prediction and Uncertainty for Underwater 3-D Reconstruction. *IEEE Trans. Instrum. Meas.* **2026**, *75*, 2505917. [CrossRef]
35. Fan, S.; Chang, J.; Wang, Z.; Ding, M.; Sun, H.; Zhao, Y. Research on Adaptive Cooperative Positioning Algorithm for Underwater Robots Based on Dolphin Group Cooperative Mechanism. *Biomimetics* **2026**, *11*, 82. [CrossRef]
36. Wei, H.; Zhang, M.; Wang, C.; Wang, J.; Xie, Z.; Hu, H.; Du, P. A novel interpretable intelligent attitude perception system for underwater vehicles based on pulsating pressure sensor array. *Ocean Eng.* **2026**, *364*, 127176. [CrossRef]

Disclaimer/Publisher's Note: The statements, opinions and data contained in all publications are solely those of the individual author(s) and contributor(s) and not of MDPI and/or the editor(s). MDPI and/or the editor(s) disclaim responsibility for any injury to people or property resulting from any ideas, methods, instructions or products referred to in the content.